THE ASTROPHYSICAL JOURNAL, 287:707–722, 1984 December 15

HIGH-VELOCITY HCO^+ IN CEPHEUS A: IONIZATION LEVELS IN HIGH-DENSITY CLUMPS WITHIN A MOLECULAR FLOW

ROBERT B. LOREN,[1] ALWYN WOOTTEN,[2] AA. SANDQVIST,[3] P. FRIBERG,[4] AND Å. HJALMARSON[4]
Received 1983 October 10; accepted 1984 June 27

ABSTRACT

High-velocity (FWZP ~ 44 km s^{-1}) HCO^+ wings have been detected in both the $J = 1$–0 and $J = 3$–2 lines toward Cep A. Modeling the intensity ratio in the wings of these two lines indicates that this emission arises in high-density (10^6 cm^{-3}) clumps within a high-velocity outflow. The highest velocity HCO^+ emission is confined to an unresolved region at the location of the IR cluster and H_2O masers. At intermediate velocities the HCO^+ emission is spatially extended, with redshifted and blueshifted lobes on opposite sides of the dense core, a bipolar pattern similar to that seen in CO emission wings. Both the HCO^+ abundance (3–6×10^{-9}) and the electron abundance ($< 10^{-8}$) in the high-velocity flow are similar to more quiescent cold molecular clouds. Such low ionization levels within the molecular flow are a condition needed for the magnetic precursor model of shock structure (Draine 1980).

Subject headings: interstellar: molecules — nebulae: general

I. INTRODUCTION

High-velocity molecular flows disclose gas swept up by stellar winds. These winds can be generated by stars with a wide range of luminosity. Moderate CO line wings arranged in a spatial pattern of oppositely directed blueshifted and redshifted lobes were identified with the modest-luminosity ($25\ L_\odot$) star IRS 5 in L1551 (Snell, Loren, and Plambeck 1980). A bipolar spatial distribution of the high-velocity CO (Erickson *et al.* 1982; Phillips, White, and Watt 1982) and HCO^+ (Olofsson *et al.* 1982) emission is also found in the high-luminosity ($10^5\ L_\odot$) cluster in OMC-1. The bipolar distribution of redshifted and blueshifted line wings arises when the outflow is channeled into oppositely directed jets by a dense circumstellar disk (Snell, Loren, and Plambeck 1980). A high-density disk, oriented perpendicular to the axis of the outflow lobes, has been resolved in the interferometric observations of SO toward OMC-1 (Plambeck *et al.* 1982). High-density clumps in the disk may be accelerated outward by the stellar wind. Evidence for these high-density disks and for clumps in the outflow may also be found in other lower luminosity outflow sources.

While CO is an ideal molecule for initially detecting outflow regions, its high optical depths ($\tau > 1$), even in the CO line wings, and the small beam filling factors of the high-velocity gas (Loren *et al.* 1981; Plambeck, Snell, and Loren 1983) limit its usefulness as a density probe of these regions. The abundant HCO^+ molecule is a better probe of both the high-density disk and the high-density outflow component since the excitation for HCO^+ emission requires densities two orders of magnitude greater than the density required to excite CO emission. High-velocity HCO^+ line wings have been detected toward OMC-1 (Turner and Thaddeus 1977), W3, Mon R2, Cep A, and NGC 2071 (Loren and Wootten 1980).

We have chosen several molecular outflows for multi-transition studies of the abundant HCO^+ and $H^{13}CO^+$ molecular ions. The results for NGC 2071 are discussed by Wootten *et al.* (1984), and the Cep A results in this paper. Observations of the high-velocity outflow source in OMC-1 in the $J = 4$–3 and $J = 3$–2 lines of HCO^+ and $J = 3$–2 HCN are given by Wootten and Loren (1984) and in H_2CO by Wootten, Loren, and Bally (1984).

II. OBSERVATIONS AND CALIBRATION

Maps of the HCO^+ and $H^{13}CO^+$ line profiles have been made in both the $J = 1$–0 and $J = 3$–2 transitions. Table 1 gives the line rest frequency, the beam size, and the efficiency of the antenna used for each observed transition. The $J = 1$–0 lines were mapped with the NRAO[5] 11 m antenna at Kitt Peak during 1980 June and 1982 June. Higher spatial resolution observations were obtained in the $J = 1$–0 HCO^+, $H^{13}CO^+$, and CO lines with the OSO[6] 20 m antenna. The OSO beamwidth at 89 GHz is 42″, and the main beam efficiency is 54%. A single-sideband (SSB) tuned cooled receiver with a 350 K noise temperature was used.

The $J = 3$–2 HCO^+ and $H^{13}CO^+$ lines were mapped with the 4.9 m MWO[7] antenna located near Ft. Davis, Texas. The beamwidth of the MWO antenna at 267 GHz is ideally matched to the NRAO antenna at 89 GHz (Table 1). Observations of the $J = 3$–2 lines were made during 1981 March–April using a cooled heterodyne mixer receiver (Erickson 1981) with typical system temperatures of 3600–6500 K. Observations using an improved tripler during 1982 January had a system temperature of 1800–2400 K at 267 GHz for measured atmospheric opacities of 0.25–0.35. A few observations of the $J = 2$–1 CO and ^{13}CO lines were also made with this receiver. Typically a linear baseline was removed from the 1 MHz

[1] Millimeter Wave Observatory, Electrical Engineering Research Laboratory, The University of Texas at Austin and McDonald Observatory.
[2] National Radio Astronomy Observatory, Charlottesville, Va. (Formerly at Owens Valley Radio Observatory and Rensselaer Polytechnic Institute.)
[3] Stockholm Observatory, Sweden.
[4] Onsala Space Observatory, Sweden.

[5] The National Radio Astronomy Observatory is operated by Associated Universities, Inc., under contract with the National Science Foundation.
[6] The Onsala Space Observatory (OSO), Chalmers University of Technology, is operated with financial support from the Swedish Natural Science Research Council. The receiver development has been sponsored by the Swedish Board for Technical Development.
[7] The Millimeter Wave Observatory (MWO) is operated by the Electrical Engineering Research Laboratory, The University of Texas at Austin, with support from the National Science Foundation and McDonald Observatory.

TABLE 1

LINE FREQUENCIES AND ANTENNA PARAMETERS

Line	Molecule	Line Frequency	Beam Size	Antenna	Adopted $\eta_C \eta_{FSS}$	Velocity Resolution (km s^{-1})
$J = 1$–0	HCO^+	89.188523	75″	NRAO	0.64	0.34 and 0.84
			42″	OSO	0.35	0.20 and 0.84
$J = 3$–2	HCO^+	267.557619	72″	MWO	0.52	0.28 and 1.12
$J = 1$–0	$H^{13}CO^+$	86.754330	77″	NRAO	0.64	0.35 and 0.85
			43″	OSO	0.35	0.20 and 0.84
$J = 3$–2	$H^{13}CO^+$	260.2554	74″	MWO	0.52	0.29 and 1.15
$J = 2$–1	CO	230.538001	81″	MWO	0.55	0.33 and 1.30
$J = 2$–1	^{13}CO	220.398714	85″	MWO	0.55	0.34 and 1.36

NOTE.—The $J = 3$–2 HCO^+ rest frequency is from Sastry, Herbst, and DeLucia 1981, and the $J = 1$–0 HCO^+ and $H^{13}CO^+$ rest frequencies are from Bogey, Demuynck, and Destombes 1981.

resolution data to establish the baseline for the 250 kHz resolution data.

The $J = 1$–0 HCO^+ emission map consists of 45 positions and the $J = 1$–0 $H^{13}CO^+$ emission map consists of 11 positions observed with the NRAO antenna. The $J = 3$–2 HCO^+ emission map consists of 14 positions, and the $J = 3$–2 $H^{13}CO^+$ emission map consists of three positions observed with the MWO antenna. The map of $J = 1$–0 CO emission consists of 65 positions made with the OSO antenna.

Calibration at NRAO and MWO antennas was achieved by synchronous detection of an ambient temperature absorber chopped against the sky. The observed line intensities for each antenna system are expressed as T_A^*, which only includes atmospheric absorption corrections. A further correction for forward scattering and spillover efficiency (η_{FSS}) relates T_A^* to T_R^* (Kutner and Ulich 1981):

$$T_R^* = T_A^*/\eta_{FSS} .$$

To find the radiation temperature, T_R—the quantity which should be used to compare lines at different frequencies—corrections must also be applied for the coupling efficiency (η_C) of the source distribution to the antenna diffraction pattern:

$$T_R = T_R^*/\eta_C = T_A^*/\eta_C \eta_{FSS} .$$

For lines at greatly different frequencies arising from a small source, it is not adequate to assume that $\eta_C = 1$ (i.e., the source is large compared with the beam pattern). A full beam map of the MWO antenna at 1.3 mm and main beam efficiency measurements at all observed frequencies have been combined with Ruze theory to calculate η_C for the observed frequencies (Mundy 1981). For example, for a source radius of 2′, the MWO antenna has $\eta_C \eta_{FSS}(267\ \text{GHz}) = 0.52$, and from the data in Ulich and Haas (1976), the NRAO antenna has $\eta_C \eta_{FSS}(89\ \text{GHz}) = 0.64$. To determine densities from the HCO^+ data requires the ratio of $J = 3$–2 to $J = 1$–0 line intensities. Fortunately, this ratio is insensitive to source size since both MWO and NRAO antennas have similar functional dependence of η_C upon source size for the appropriate frequencies and range of source sizes. For the OSO antenna we have estimated that $\eta_C \eta_{FSS}(89\ \text{GHz}) = 0.35$, but because of the large difference in beam size, these data cannot be directly compared with the MWO data. Slightly different efficiencies were used in preliminary reports of these observations (Sandqvist *et al.* 1982*a*, *b*), which resulted in somewhat higher density estimates.

III. PREVIOUS OBSERVATIONS OF CEPHEUS A

In the CO map of the Cep OB3 association Sargent (1977) identified a hot spot, referred to as Cep A, that has self-reversed CO line profiles possessing broad wings coincident with a dense core in the cloud. A variety of other signposts of star formation are found associated with the Cep A cloud (Table 2). Beichman, Becklin, and Wynn-Williams (1979) have found three strong compact 6 cm continuum sources associated with a spatially extended ($\sim 9''$), cold ($T_{color} \sim 88$ K) 20 μm source in the cloud core. An OH maser (Rodríguez *et al.* 1980; Norris 1980) and a cluster of H_2O maser emission spots (Lada *et al.* 1981) are concentrated around two of the strong continuum sources.

Far-infrared observations (Koppenaal *et al.* 1979; Evans *et al.* 1981) measure a luminosity from the region of $2.5 \times 10^4\ L_\odot$, which could be supplied by either a single B0 V star or a small cluster of slightly cooler stars. The dust temperatures range from 40 to 50 K (Evans *et al.* 1981). Phillips *et al.* (1981) deduced a gas temperature of $T_K = 33 \pm 11$ K from modeling of CO line profiles. An independent measurement of $T_K = 30 \pm 5$ K comes from observations of CH_3CCH (Mundy and Loren 1984).

Rodríguez, Ho, and Moran (1980) mapped the Cep A molecular outflow in the $J = 1$–0 CO line. They found that the velocity extent of the wings, toward the core, is ~ 45 km s^{-1}, and lobes of redshifted and blueshifted high-velocity CO occur, respectively, on the northwest and east sides of the core. The origin of the outflow lies near the H_2O masers and the radio continuum sources. Loren and Wootten (1980) found high-velocity $J = 1$–0 HCO^+ emission toward Cep A, with a velocity extent comparable to the CO emission.

A small nebulosity (GGD 37)[8] found by Gyulbudaghian, Glushkov, and Denisyuk (1978) provides optical evidence of an interaction of an outflow and the molecular cloud. The nebulosity lies, not at the dense Cep A core, but $\sim 2'$ *west* of the core, and the optical spectra in parts of this nebulosity (Levreault 1982) show strong [O I] and [S II] emission lines characteristic of a Herbig-Haro object. These forbidden emission lines are produced in a low-excitation shock (Dopita 1978); e.g., where a stellar wind encounters dense molecular

[8] GGD 37 is not to be confused with the Herbig-Haro object HH 37 in Orion.

TABLE 2

OBJECT POSITIONS IN THE CEPHEUS A CORE

Object	Beam Size	α(1950)	δ(1950)	Reference
Infrared				
20 μm	6″.5	$22^h54^m19^s.3$	+61°45′51″.5	Beichman, Becklin, and Wynn-Williams 1979
2 μm	15″	22 54 19.5 ± 0.7	61 45 46 ± 5	Bally and Lane 1982
2.12 μm H_2	15″	22 54 24.2	61 46 03	Bally and Lane 1982
85–150 μm	4′.5	22 54 42	61 47 12	Koppenaal *et al.* 1979
125 μm	50″	22 54 21.7 ± 2.1	61 45 43 ± 15	Evans *et al.* 1981
Radio Continuum				
4.9 GHz R1	1″	22 54 19.2	61 45 44	Beichman, Becklin, and Wynn-Williams 1979
R2	1″	22 54 19.0	61 45 47	Beichman, Becklin, and Wynn-Williams 1979
R3	1″	22 54 19.6	61 45 54	Beichman, Becklin, and Wynn-Williams 1979
4.9 GHz	1″	22 54 19.2 ± 0.07	61 45 44.1 ± 0.5	Rodríguez *et al.* 1980
0.6–14.7 GHz	0′.9–2′.6	22 54 19.0 ± 0.5	61 45 42 ± 4	Harten, Thum, and Felli 1981
1.4 GHz	30″	22 54 20.0	61 45 44.3	Hughes and Wouterloot 1982
1.4 GHz (HH obj.)	30″	22 54 09.6	61 45 45	Hughes and Wouterloot 1982
Molecular Peaks				
CO	2′.3	22 54 25	61 44 36	Sargent 1977
NH_3	2′.2	22 54 18	61 46 00	Brown *et al.* 1981
HCO^+ $J = 1$–0	1′.3	22 54 21.3	61 45 43	This paper
HCO^+ $J = 3$–2	1′.2	22 54 19.2	61 46 00	This paper
$H^{13}CO^+$ $J = 1$–0	1′.3	22 54 19.2	61 46 00	This paper
H_2O maser A	...	22 54 19.04	61 45 48	Lada *et al.* 1981
H_2O maser B	...	22 54 19.21	61 45 44.2	Lada *et al.* 1981
OH maser	...	22 54 19.06 ± 0.09	61 45 44.7 ± 0.8	Norris 1980

gas. These are several stars and a radio continuum source (Hughes and Wouterloot 1982) in the vicinity of the HH objects, but displaced from the core sources. Additional evidence of high-temperature shock-excitation is found in the detection of 2.1 μm H_2 emission in a region to the *east* of the Cep A H_2O masers, coincident with the center of the blue-shifted high-velocity CO lobe (Bally and Lane 1982). Bally and Lane suggest that foreground extinction masks any 2.1 μm H_2 emission from the more distant, western, redshifted CO lobe.

IV. HCO^+ AND $H^{13}CO^+$ OBSERVATIONS

a) *Line Profiles toward the Cloud Core*

Because of the different optical depths in different lines or parts of the line profile and excitation requirements, the four lines of the $J = 1$–0 and $J = 3$–2 (for both HCO^+ and $H^{13}CO^+$) probe conditions in different parts of the molecular cloud. Both low optical depth $H^{13}CO^+$ lines probe the dense core. The higher optical depth in the wings of both the HCO^+ lines allows the high-density outflow to be probed. The $J = 1$–0 resonance line of HCO^+ also probes the modest-density foreground gas in a narrow range of velocities near the line center.

Figure 1 shows that the MWO line profiles of CO and HCO^+, toward the core of Cep A, have comparably broad high-velocity wings: 45 km s^{-1} for the $J = 2$–1 CO and 38 km s^{-1} for the $J = 3$–2 HCO^+. Figure 2 shows all of the HCO^+ and $H^{13}CO^+$ line profiles toward the core of the Cep A cloud. The strong high-velocity HCO^+ emission, especially in the $J = 3$–2 line, which requires densities a factor of 100 greater than CO emission, reveals the presence of a very high density component within the molecular outflow. Evidence of even higher densities, near the outflow source, is provided by the H_2O maser emission, whose range of velocity components coincides with the velocity extremes in the broad HCO^+ emission. A comparison of the $J = 1$–0 HCO^+ wings in the core line profiles (Fig. 2), taken with two different beam sizes, reveals that part of the high-velocity emission is spatially unresolved, since the wings (especially the blue wing) are stronger in the smaller OSO beam than in the larger NRAO beam. The detectable velocity extent of the $J = 1$–0 HCO^+ emission is 44 km s^{-1} in the 42″ OSO beam compared with 38 km s^{-1} in the 75″ NRAO beam.

The shapes of the two $H^{13}CO^+$ line profiles are similar (Fig. 2), centered at -11 km s^{-1} and 3–4 km s^{-1} wide. There is no evidence for broad wings in either $H^{13}CO^+$ line profile ($\Delta V_{FWZP} \sim 5$ km s^{-1}), although they become narrower at positions displaced from the cloud core (Table 3). This confirms the expected low optical depth of the entire $H^{13}CO^+$ line profile and the HCO^+ line wings. As a result, the ratio of intensities from two lines should be a good estimate of the density: the $H^{13}CO^+$ lines for the cloud core and the HCO^+ wings for the outflow material.

The central portion of the HCO^+ lines cannot be used to form an accurate line ratio since the $J = 1$–0 HCO^+ line profile is affected by the foreground optically thick low-excitation gas, while the $J = 3$–2 line remains unaffected. The narrow minimum at -9.5 km s^{-1} can be identified as absorption by comparing the $J = 1$–0 HCO^+ and $H^{13}CO^+$ line profiles (Fig. 2). The higher velocity of the HCO^+ absorption feature relative to the $H^{13}CO^+$ peak indicates a 1.6 km s^{-1} motion of the absorbing foreground layer toward the dense core. The $J = 1$–0 and $J = 2$–1 CO line profiles in a typical molecular cloud differ in only one respect, the greater depth of the $J = 2$–1 CO self-reversal (Loren *et al.* 1981). The situation is quite different for the HCO^+ lines, as illustrated by the comparison of the $J = 1$–0 and $J = 3$–2 HCO^+ lines toward the core of Cep A (Fig. 2). At displacements of more than 4 km s^{-1} from the -11 km s^{-1} line center, the high-velocity wings of the two line profiles are virtually identical. The greatest

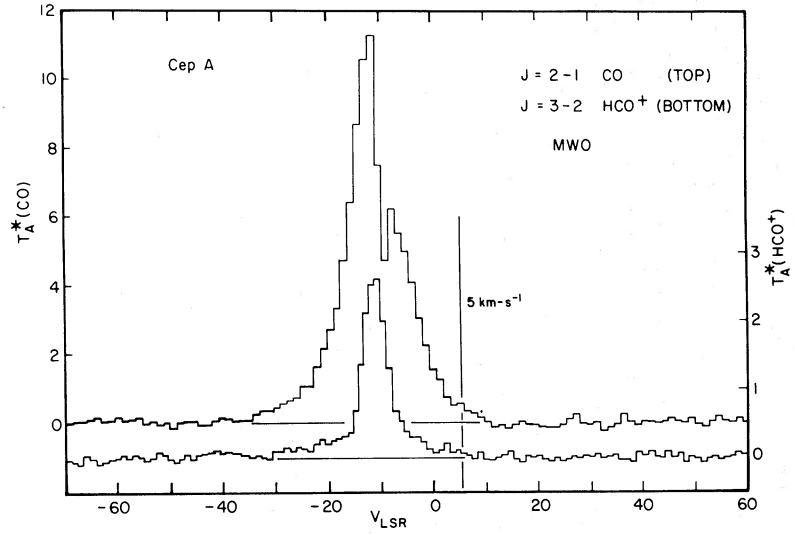

FIG. 1.—A comparison of the MWO $J = 2$–1 CO and J = 3–2 HCO^+ line profiles toward Cep A [$\alpha(1950) = 22^h54^m21^s.3$, $\delta(1950) = 61°45'43''$]. The vertical line marks the velocity at which a narrow spike occurs in the $J = 1$–0 CO line profile. There is no evidence for this component in either the $J = 2$–1 CO or the $J = 3$–2 HCO^+. The high-velocity wings in the HCO^+ line extend over nearly as large a velocity range as the CO emission.

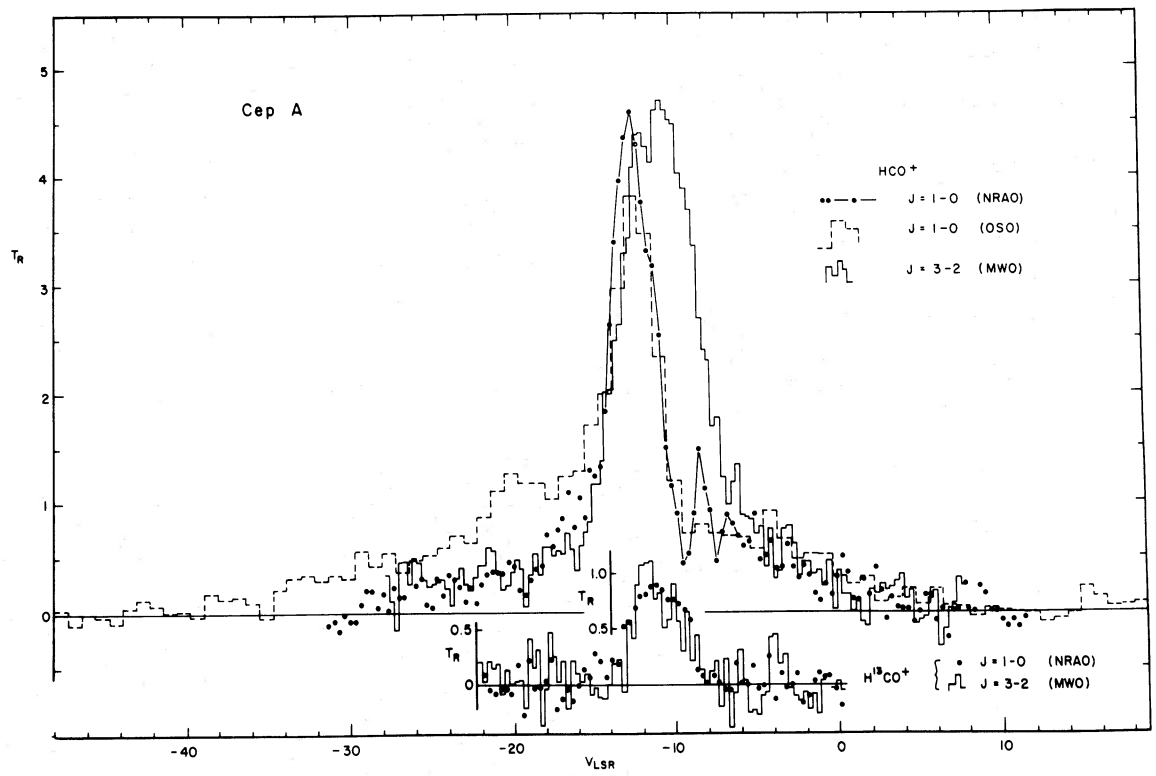

FIG. 2.—The line profiles of HCO^+ and $H^{13}CO^+$ observed toward the Cep A core [$\alpha(1950) = 22^h54^m21^s.3$, $\delta(1950) = 61°45'43''$]. The $J = 3$–2 lines of HCO^+ and $H^{13}CO^+$ were observed with the MWO antenna and the $J = 1$–0 HCO^+ and $H^{13}CO^+$ were observed with both the NRAO and OSO antennas. The beam sizes are nearly matched for the MWO (72″) and NRAO (75″) antennas at the observed frequencies. A self-absorption feature appears at -9.5 km s^{-1} in only the $J = 1$–0 HCO^+ line observed with high spectral resolution. The baselines for the HCO^+ lines are established with additional spectral coverage outside the velocity range shown. Both $H^{13}CO^+$ lines are narrow compared with the HCO^+, and no self-absorption is evident.

TABLE 3

H^{13}CO$^+$ DATA

Position	T_A^*	V_{LSR}	ΔV	rms	T_R
		J = 1–0 NRAO			
ON[a]	0.55	−10.9	4.5	0.09	0.86
CO peak (1′.1S-0′.5E)	0.25	−12.2	1.7	0.09	0.39
1′E	0.44	−11.7	3.1	0.04	0.69
1′W	0.80	−10.0	2.1	0.07	1.25
1′N	0.68	−10.7	3.5	0.13	1.1
2′W	0.45	−10.2	3.1	0.14	0.7
1′N-1′W	0.77	−10.0	1.2	0.14	1.2
1′S-1′E	≤0.37	−10.5	0.5	0.16	≤0.57
1′N-1′E	0.38	−11.2	2.8	0.09	0.59
2′N	0.29	−11.2	1.9	0.11	0.45
2′N-2′W	<0.2	...	...	0.17	<0.3
		J = 1–0 OSO			
ON[a]	0.45	−11.1	3.7	0.09	0.83
		J = 3–2 MWO			
ON[a]	0.50	−11.3	3.2	0.10	0.96
0′.5E	0.22	−10.7	3.4	0.13	0.42
0′.5W	0.53	−11.1	2.1	0.10	1.0

[a] Reference ON position is $\alpha(1950) = 22^h54^m21^s.3$, $\delta(1950) = 61°45'43''$.

difference occurs around the velocity of the J = 1–0 HCO$^+$ self-reversal (−9.5 km s^{-1}), where the J = 1–0 intensity is less than 0.5 K, while the J = 3–2 line is very strong, 3–4 K. The low density of the foreground gas, which produces the absorption feature in the J = 1–0 HCO$^+$ and CO lines, cannot populate the levels to produce J = 3–2 HCO$^+$ emission but can produce J = 2–1 CO emission. The emission at −9.5 km s^{-1} in the J = 3–2 HCO$^+$ line comes entirely from the high-density core. The J = 3–2 HCO$^+$ line is broader than the H^{13}CO$^+$ lines because the J = 3–2 HCO$^+$ transition is optically thick in the core even though no absorption feature is evident.

b) *Distribution of Quiescent* HCO$^+$

The J = 3–2 HCO$^+$ line could be used to study the distribution of quiescent cloud material, but the J = 1–0 HCO$^+$ observations have a much better spatial coverage and will be used, keeping in mind the problems with foreground absorption. The spatial peak of the J = 1–0 HCO$^+$ line integrated over the central interval −13.4 to −9.2 km s^{-1} in Figure 4 is near the position of the far-infrared emission (Evans *et al.* 1981), i.e., slightly to the east of the H_2O masers. The elongation of the HCO$^+$ distribution from the NE to the SW could be the result of the self-absorption or the flattening of the core into a disk. The major axis of the emission lies nearly perpendicular to the east-west axis defined by the lobes of redshifted and blueshifted CO gas found by Rodríguez, Ho, and Moran (1980). If a disk were present, it could channel the molecular outflow along its symmetry axis, the direction of minimum density.

The more limited H^{13}CO$^+$ and J = 3–2 HCO$^+$ emission maps, unaffected by foreground absorption, provide an unbiased position for the high-density core. Both the integrated J = 1–0 H^{13}CO$^+$ and the integrated J = 3–2 HCO$^+$ emission are centered at $\alpha(1950) = 22^h54^m19^s.2$, $\delta(1950) = 61°46'00''$, coincident with the H_2O masers, etc. (Table 2). The extent of the half-maximum J = 1–0 H^{13}CO$^+$ intensity contours is 2′ × 3′. At a distance of 730 pc (Garmany 1973) the deconvolved core size is 0.34 × 0.59 pc. The limited J = 3–2 HCO$^+$ emission map tends to confirm a NE-SW elongation of the dense material in the core of the cloud.

c) *Quiescent Cloud Velocity Field*

Because of the high optical depth of low-density foreground gas, which absorbs the core emission profiles, the J = 1–0 HCO$^+$ line, like CO, is not a good probe of the intrinsic velocity field of the core of the cloud. In contrast, the H^{13}CO$^+$ lines and the J = 3–2 HCO$^+$ line appear unaffected and should accurately measure the line-of-sight velocities. There are variations of both central V_{LSR} and line width of the H^{13}CO$^+$ lines (Table 3) and the J = 3–2 HCO$^+$ lines (Table 4) across the cloud. At all positions the H^{13}CO$^+$ line profiles are symmetric and can be best fit by a single Gaussian. Some of the J = 3–2 HCO$^+$ line profiles are slightly asymmetric, especially to the west of the core, and are better fit by a two-component Gaussian (with mean velocities of −11.4 and −9.2 km s^{-1}). For the single-component H^{13}CO$^+$ fits the V_{LSR} gradient across the (4′ = 0.8 pc) core of the cloud is 2.2 km s^{-1} pc^{-1} in an east-west direction. Some of this velocity gradient could be produced by the changing relative intensities of two velocity components. This velocity gradient has the same sense as the velocity shifts of the high-velocity gas (discussed in the next section), i.e., higher V_{LSR} to the west.

d) *Spatial Distribution of High-Velocity* HCO$^+$ *Outflow*

Because of the possible complexity of the velocity field, the full line profiles at all positions need to be viewed as an ensemble. This is partially accomplished with the east-west spatial versus velocity map of the J = 1–0 and J = 3–2 HCO$^+$ emission given in Figure 3. From this figure we can see that the broad HCO$^+$ wings are spatially extended, and that there is a shift of the wing velocity across the cloud core; the blueshifted emission occurs on the east, and the redshifted emission occurs on the west side of the core. A comparison of the maps in the two lines in Figure 3 illustrates the differences in the optical depth of the foreground gas between the two transitions. The self-absorption feature at −9.5 km s^{-1} in the J = 1–0 HCO$^+$ line (indicated by the dashed line) is limited to the core of the cloud, but there is no absorption evident in the J = 3–2 HCO$^+$ line at any velocity or position.

Differences in the spatial distribution of the J = 1–0 HCO$^+$ emission as a function of velocity are displayed in the nine individual velocity interval maps in Figure 4, which cover the

TABLE 4

MWO J = 3–2 HCO$^+$ DATA

Position	T_A^*	V_{LSR}	ΔV	rms	T_R	Alternate Fit Velocities
ON	2.4	−10.7	5.5	0.07	4.6	...
0′.5N-0′.5E	2.5	−11.2	4.3	0.3	4.8	...
0′.5N	2.4	−10.7	4.6	0.4	4.6	−11.9 and −9.5
0′.5N-0′.5W	1.8	−10.1	5.2	0.4	3.5	...
0′.5W	2.4	−10.2	5.7	0.3	4.6	−12.2 and −9.1
0′.5S-0′.5W	2.1	−10.2	5.9	0.4	4.0	−11.7 and −8.7
0′.5S	1.7	−10.9	5.0	0.4	3.3	...
0′.5E	2.0	−11.0	4.6	0.2	3.9	...
1′E	1.3	−10.6	5.0	0.25	2.5	...
1′.5E	1.3	−11.5	4.0	0.3	2.5	...
2′E	0.9	−10.7	4.0	0.1	1.7	...
1′W	2.7	−9.3	4.3	0.1	5.2	−10.2 and −8.9
1′.5W	1.4	−10.1	2.6	0.3	2.7	...
2′W	1.1	−9.8	2.2	0.15	2.1	−11.2 and −9.6

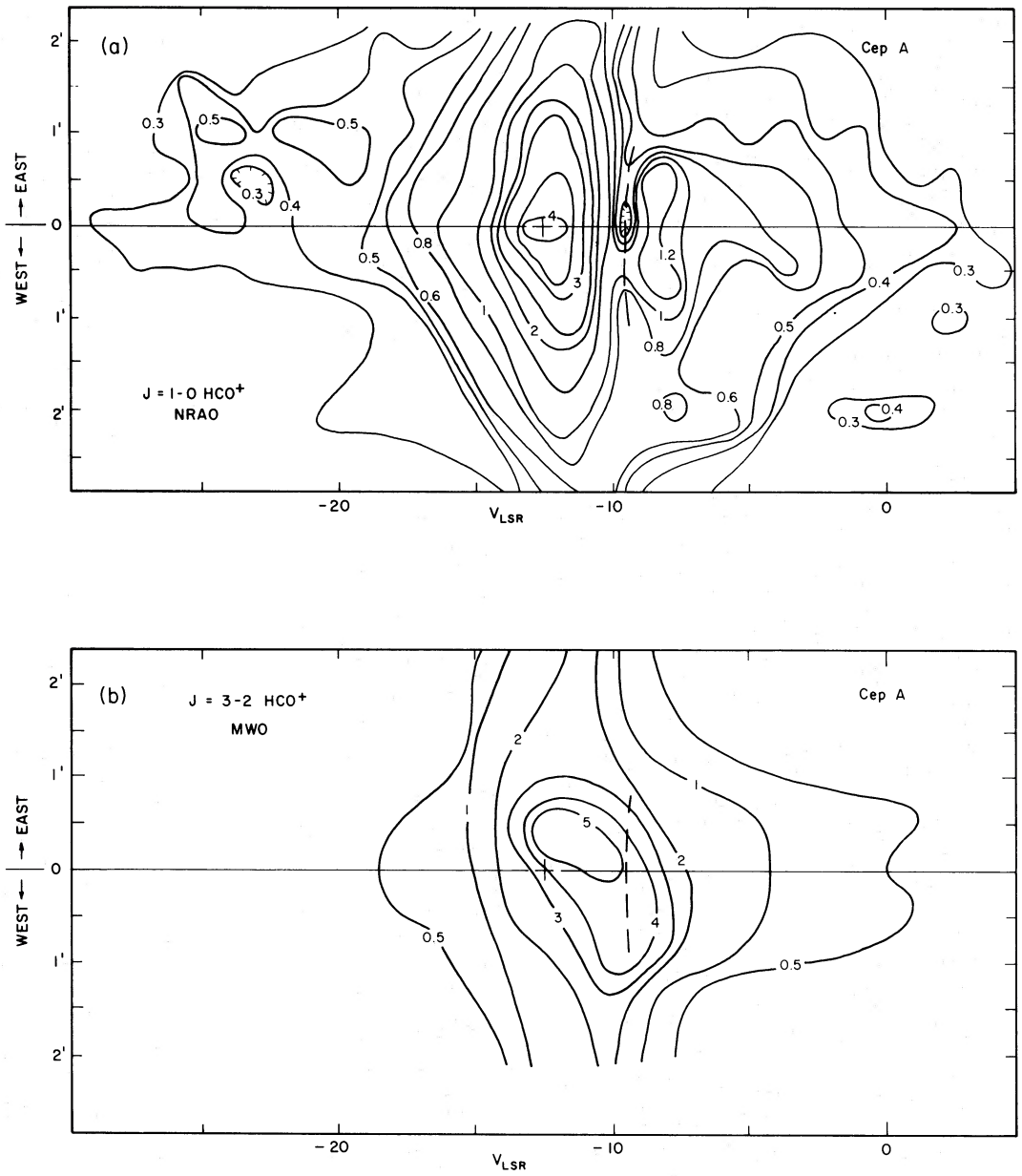

FIG. 3.—The V_{LSR} vs. right ascension through the core of the Cep A cloud for the (*a*) $J = 1$–0 HCO^+ and (*b*) $J = 3$–2 HCO^+. The extent and velocity of the self-absorption defined by the $J = 1$–0 HCO^+ are indicated in Figs. 3*a* and 3*b* by a vertical dashed line.

V_{LSR} range from -30.2 to 7.6 km s^{-1}. The modest bipolarity of the high-velocity HCO^+ emission regions is apparent only at intermediate velocity intervals; for example, blueshifted gas (-26.0 to -17.6 km s^{-1}) occurs 1′ to the east, and redshifted gas (-5.0 to 3.4 km s^{-1}) lies from 0.′5 to 2′ to the west of the H_2O masers (also see Fig. 5). Even within these velocity intervals the intensity of the high-velocity HCO^+ emission is strong at the position of the H_2O masers. At the very highest velocity intervals in Figure 4 (-30.2 to -26.0 km s^{-1} and 3.4 to 7.6 km s^{-1}) both the blueshifted and redshifted HCO^+ emission regions have the same spatial extent and are centered about half a beamwidth to the east of the H_2O masers. The distribution of redshifted HCO^+ emission includes a semidetached lobe 2′ west of the H_2O masers, in the vicinity of the HH object emission (see especially the interval -0.8 to 3.4 km s^{-1}).

In Figure 4 the top (blueshifted) and bottom rows (redshifted) of individual velocity maps of HCO^+ emission can be compared with maps of CO emission, in similar velocity intervals, given by Ho, Moran, and Rodríguez (1982). The centers of the distributions of blueshifted ($V_{LSR} = -30.2$ to -17.6 km s^{-1}) CO and HCO^+ emission coincide at a position to the east or northeast of the H_2O masers. One difference is that at the position of the H_2O masers, the CO intensity is very much reduced relative to the peak, while the HCO^+ emission has similar intensities at both positions. In the -17.6 to -13.4 km s^{-1} velocity interval (not given in CO by Ho *et al.*) the HCO^+ emission is strongest at the H_2O masers. The redshifted HCO^+ and CO emission in the intervals -5.0 to -0.8 km s^{-1} and -0.8 to 3.4 km s^{-1} peaks at the H_2O maser, and a second, separate region of weaker HCO^+ emission occurs about 2′W

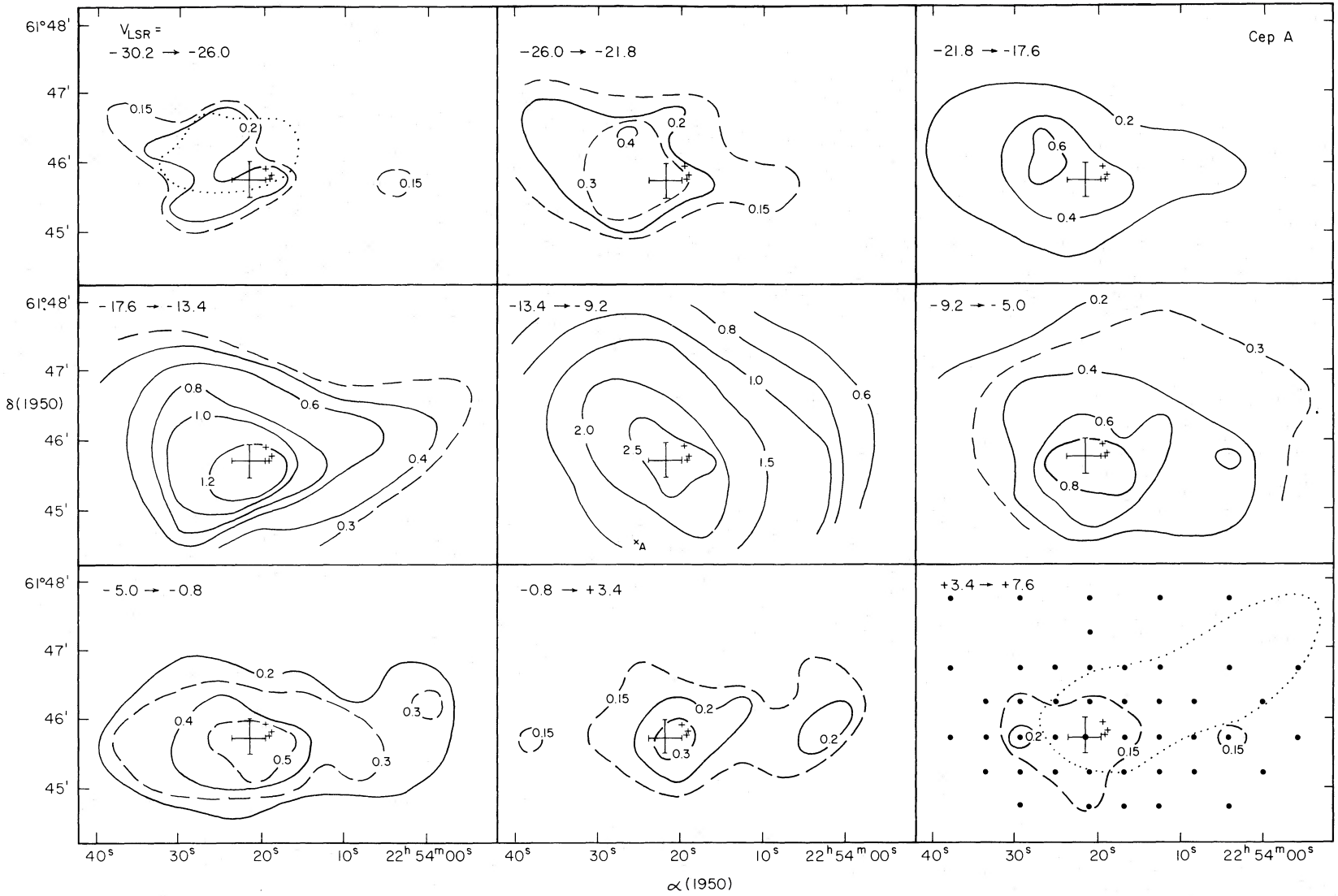

FIG. 4.—The spatial distribution of $J = 1$–0 HCO^+ emission for nine different velocity intervals. The contours are values of $T_R(J = 1\text{–}0\ HCO^+)$. The large cross in each panel corresponds to the position of the 125 μm peak (Evans *et al.* 1981). The three small crosses correspond to the 6 cm radio continuum sources (Beichman, Becklin, and Wynn-Williams 1979). The H_2O masers coincide with the two southernmost radio sources. The filled circles in the lower right panel indicate the positions that were observed. The dotted contour lines in the upper left and lower right panels correspond, respectively, to the blueshifted and redshifted CO lobes, from Rodriguez, Ho, and Moran (1980). The original large-beam CO position of Sargent (1977) is indicated by an *A* in the central panel.

of the core, near the HH objects. A significant difference occurs between the HCO^+ and CO maps in the highest velocity redshifted interval (3.4–7.6 km s^{-1}). There is little or no HCO^+ at any positions to the NW, a region where strong redshifted high-velocity CO emission is found. This is the only redshifted velocity interval in which the CO is clearly strongest at a position other than the core, and it is this interval which contains an extraneous low-density CO emission component at 5 km s^{-1} (Appendix). The concentration of both the highest velocity redshifted and blueshifted HCO^+ emission close to the H_2O masers can be explained by higher core densities and/or a greater concentration of dense clumps. This shows up better in the HCO^+ maps since higher densities are required to excite HCO^+ compared with CO.

We need to reduce this wealth of information to a map which represents just the integrated high-velocity flow. The limits on integration, to exclude quiescent cloud emission, are clearly subjective. For the Cep A $J = 1$–0 HCO^+ emission, velocities within ± 3.8 km s^{-1} of line center [$V_{LSR}(H^{13}CO^+) = -11.1$ km s^{-1}] are excluded. As a result, high-velocity gas at low *projected* velocity will not be included. Integration extends to the velocity at which $T_R(HCO^+, J = 1\text{–}0)$ falls below 0.3 K. At each observed position the integrated intensity is calculated for both the redshifted and blueshifted $J = 1$–0 HCO^+ line wings. Figure 5 shows these distributions. The blueshifted high-velocity gas (Fig. 5*a*) peaks at the dense core but remains strong in a plateau extending 1′ to the east. The blueshifted gas is not found exclusively in the eastern part of the cloud. There is an extension of the contours at the level of 1 K km s^{-1} that peaks near the HH objects about 2′ west of the core. In contrast, the integrated blueshifted emission drops to negligible levels by 1′S or 1′N of the cloud core. Figure 5*b* shows that the redshifted HCO^+ line wings are also strongest at the core. There is also a semidetached lobe of redshifted HCO^+ emission, to the west of the core, that also peaks near the HH objects. The presence of both blueshifted and redshifted high-velocity emission near the HH objects suggests the presence of a second outflow source embedded in a dense condensation near the HH objects. A radio continuum source (Hughes and Wouterloot 1982), indicated by a triangle in Figure 5, found near the HH objects is a candidate for powering the flow. The coincidence of the blueshifted HH object emission lines and the redshifted CO to the NW can be attributed to this source rather than to the one embedded in the Cep A dense core.

e) A Second Outflow Source?

To investigate whether there is a secondary outflow source in the vicinity of the HH objects, we have mapped the $J = 1$–0 CO line toward Cep A with the OSO 20 m antenna. Most of these results will be reported in a later paper. Figure 5*c* shows the distribution of high-velocity CO in a blue and a red velocity interval. These high-resolution observations show that the bipolar outflow in the Cep A core is much more spatially confined than indicated in the Rodríguez *et al.* (1980) CO maps. A distinctly separate region of high-velocity flow is found near the HH objects. There is marginal evidence of some blueshifted CO in the vicinity of the Hughes and Wouterloot (1982) radio continuum source and of strong redshifted CO extending westward from the HH objects.

V. INTERPRETATION

The information in the HCO^+ and $H^{13}CO^+$ line profiles will be used to determine the physical conditions (densities,

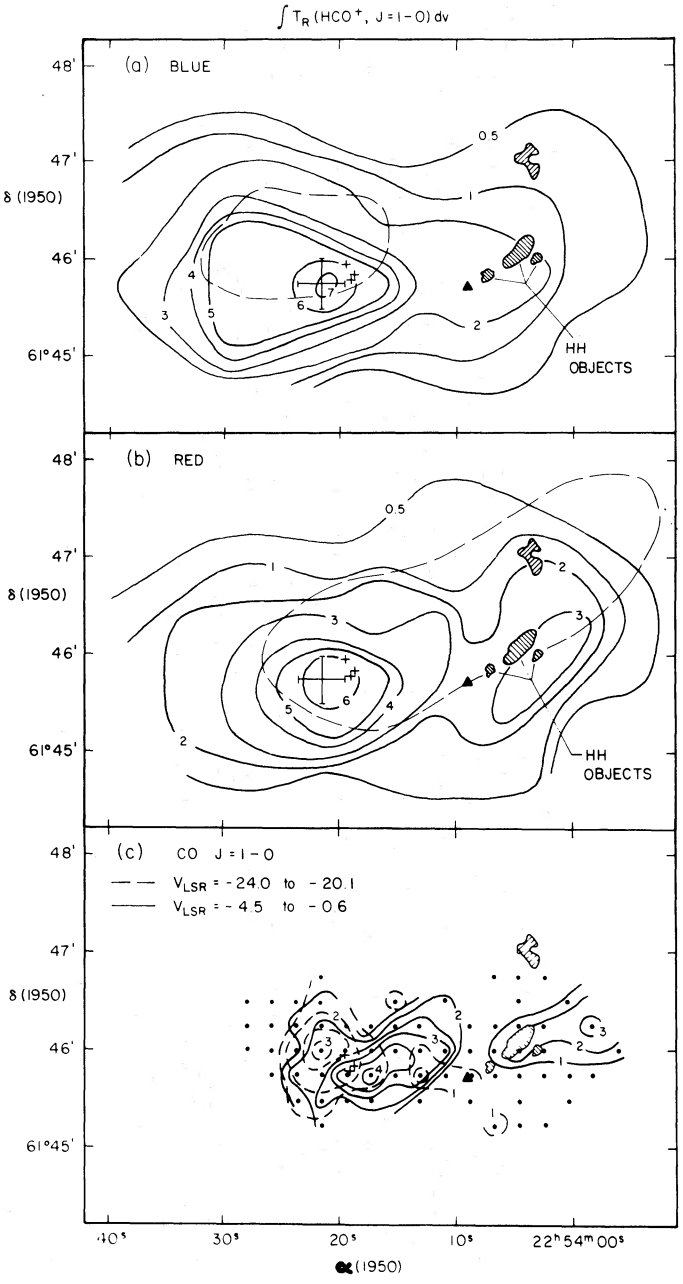

Fig. 5.—The spatial distribution of the integrated (*a*) blueshifted and (*b*) redshifted HCO^+ toward Cep A. In both panels the corresponding spatial extents of the blueshifted and redshifted $J = 1$–0 CO emission (Rodríguez, Ho, and Moran 1980) are shown by the dashed contours. The large cross indicates the position of the far-infrared source, and the small crosses indicate the 6 cm radio continuum sources. The H_2O masers coincide with the two southernmost radio sources. The solid triangle corresponds to a separate continuum source found by Hughes and Wouterloot (1982). Cross-hatching indicates optical nebulosity. The lower region of nebulosity, near the continuum source, consists of several bright condensations. Some, but not all, of these condensations have optical spectra that identify them as HH objects (Levreault 1982). Fig. 5*c* shows high angular resolution T_A^*/η_{MB} ($\eta_{MB} = 0.30$ at 115 GHz) $J = 1$–0 CO observations (OSO) of the redshifted gas (*solid contours*) and blueshifted gas (*dashed contours*). The other symbols are as above.

abundances, ionization levels, inhomogeneities, and flow energetics) in the dense core and outflow regions.

a) *Core Density and Mass*

The kinetic temperature of the core of Cep A is 35 K (Phillips *et al.* 1981). The core density is found by matching the intensity ratio at the peak of the $J = 1$–0 and $J = 3$–2 $H^{13}CO^+$ lines (Fig. 2) to a grid of large velocity gradient (LVG) radiative transfer models (Loren *et al.* 1984). These LVG models use the collision rates given by Green (1975) and a dipole moment of 3.3 debyes (Woods *et al.* 1975). The somewhat larger dipole moment calculated by Haese and Woods (1979) would lead to larger LVG model densities. At $T_k = 35$ K the best fit is at a density of 7.5×10^5 cm^{-3}. This density is much greater than the core density of 10^4 cm^{-3} estimated from NH_3 observations (Ho, Moran, and Rodríguez 1982). Evans (1980) noted the correlation between estimated cloud densities and the characteristic density (n^*) at which the collisional excitation rate balances the spontaneous decay rate in the molecular transitions used to estimate density. For the $(J, K) = 1, 1$ NH_3 line, n^* is only 1.5×10^3 cm^{-3}, while for the $J = 1$–0 HCO^+ line, $n^* = 1.5 \times 10^5$ cm^{-3}, and for the $J = 3$–2 HCO^+ line, $n^* = 7 \times 10^6$ cm^{-3}. A density of only 10^4 cm^{-3} in the Cep A core (Ho, Moran, and Rodríguez 1982) is inadequate to sufficiently excite the $J = 3$–2 HCO^+ or $H^{13}CO^+$ emission to the observed intensity relative to the $J = 1$–0 emission, independent of abundance. Therefore, a high-density component ($\sim 10^6$ cm^{-3}) must occur in the cloud core, but it does not necessarily fill the entire beam. The lower density gas within the beam dominates the observed NH_3 emission. The core mass would be uncomfortably large (1300 $M_\odot$) for a density of 7.5×10^5 cm^{-3} over the entire core. The 20 $M_\odot$ core mass, derived from the NH_3 observations (Ho, Moran, and Rodríguez 1982), would require a very high ($\sim 50\%$) efficiency for conversion of gas into stars, for a core which has already formed several massive stars (i.e., a B0 star has $M_* = 20\ M_\odot$). The LVG analysis of the HCO^+ line ratio derives a volume density of colliding particles with an unknown filling factor. In contrast, the analysis of the NH_3 data first derives the optical depth and column densities and then with an assumed source size estimates the beam-averaged line-of-sight density. As a result, when it is assumed that the region has a uniform density in a spherically symmetric distribution, the mass derived from HCO^+ data is an overestimate—and from the NH_3 it is an underestimate—of the true mass of an inhomogeneous region. The difference between these two mass estimates can be reconciled by a suitable filling factor for the high-density gas (~ 0.015). If the $H^{13}CO^+$ gas is thermalized at 35 K, then using the observed $H^{13}CO^+$ line intensity, the minimum filling factor is 0.03, and the minimum core mass is $\sim 40\ M_\odot$. A summary of the characteristics of the dense core is given in Table 5.

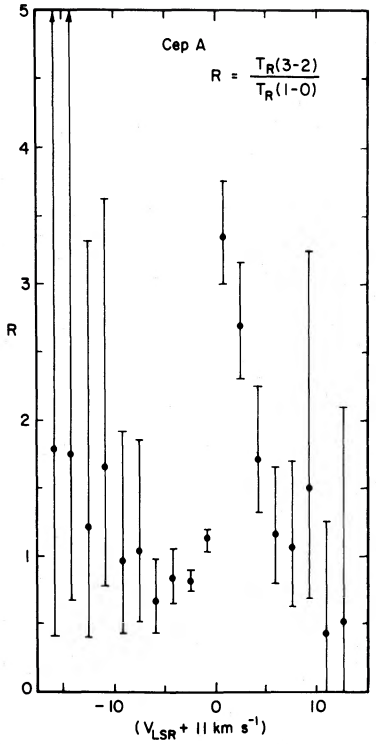

FIG. 6.—The ratio $R = T_R(3\text{–}2)/T_R(1\text{–}0)$ across the HCO^+ line at the core position [$\alpha(1950) = 22^h54^m21^s.3$, $\delta(1950) = 61°45'43''$]. The error bars correspond to a 0.10 K rms for the $J = 1$–0 line and a 0.15 K rms for the $J = 3$–2 line.

b) *Density of the High-Velocity Material*

The density of the high-velocity outflow is determined by matching the intensity ratio (R) of the $J = 3$–2 to the $J = 1$–0 HCO^+ line wings to that predicted by LVG radiative transfer models where excitation is provided by collisions and trapped radiation (Loren *et al.* 1984). In Figure 6, the observed variation of R, as a function of velocity, is shown toward the core of Cep A. The rms noise is 0.10 K for the $J = 1$–0 HCO^+ line and 0.15 K for the $J = 3$–2 HCO^+ line. The error bars in Figure 6

TABLE 5

PHYSICAL CHARACTERISTICS OF THE CEPHEUS A CORE

Observed core angular size from integrated $H^{13}CO^+$ intensities	2′ × 3′
Deconvolved linear dimensions	1.′6 × 2.′7 = 0.34 × 0.59 pc
r_{core} (radius of equivalent sphere)	0.20 pc
Core density:	
HCO^+	1×10^6 cm^{-3}
$H^{13}CO^+$	7.5×10^5 cm^{-3}
$H^{13}CO^+$ line center gradient	2.2 km s^{-1} pc^{-1}
$dV/dR = [\Delta V(H^{13}CO^+)]/2r_{core}$	11 km s^{-1} pc^{-1}
$X(H^{13}CO^+)$ from LVG model	10^{-11}
Core mass:	
$H^{13}CO^+$	$\sim 1300\ M_\odot$, upper limit
NH_3	$20\ M_\odot$, lower limit

correspond to a 1 σ error in both lines. Excluding the self-absorbed parts of the lines, the most representative value of the ratio is ~ 1.0, with the 1 σ limits for both lines at $R = 0.6$ and 2.0.

At a kinetic temperature of $T_k = 35$ K, the $R \approx 1$ HCO^+ intensity ratio requires a density of 7×10^5 cm^{-3}, a result that is fairly insensitive to the HCO^+ abundance. For optically thin conditions the range of line intensity ratio from 0.6 to 2.0 corresponds to the density range from 3×10^5 to 1.5×10^6 cm^{-3}. The effect of increasing the kinetic temperature of the region emitting the HCO^+ wings is to decrease the required density (e.g., at 90 K the ratio $R = 1$ requires 4×10^5 cm^{-3}).

The values of R in the line wings decrease slightly at positions away from the core. At the position 1'E of the core, $R = 0.5$; at 1'W, $R = 0.9$, and at 2'W, $R = 0.6$. These values indicate that although the density in the outflow is decreasing, it is still high ($> 10^5$ cm^{-3}) at positions removed from the source of the flow. There is no systematic variation of R with velocity in the high-velocity gas (within the observational errors). This suggests that both the intermediate- and high-velocity emission arise in regions of similar density.

The observed HCO^+ line intensity ratios must arise in a higher density component of the outflow than indicated by previous CO observations. The density producing the high-velocity HCO^+, required by the excitation models, is also considerably higher than that calculated from the observed HCO^+ column density and the apparent size of the outflow region, indicating a high degree of density contrast.

c) *High-Velocity* HCO^+ *and* x_e *Abundances*

The abundance of HCO^+, $X(HCO^+)$, in the high-velocity outflow cannot be accurately determined from the LVG models. Typical dark cloud HCO^+ abundances may be inappropriate, since $X(HCO^+)$ could decrease in the shock because of greater recombination at high densities and temperatures or it could increase because of enhanced cosmic-ray ionization (Elitzur 1983). One means of estimating $X(HCO^+)$ is by comparing the column density of high-velocity HCO^+ with the column density of a molecule whose abundance is expected (it is hoped) to be unchanged by the passage of the shock (e.g., Kuiper, Zuckerman, and Rodriguez-Kuiper 1981). In the absence of detailed knowledge of the excitation of each molecule, lines of similar excitation requirements should be compared. The ratio of column densities is obtained from the ratio of two optically thin emission lines that are also assumed to arise in a common volume.

For the Cep A high-velocity gas, the line wing intensities of the $J = 1$–0 HCO^+ and $J = 2$–1 ^{13}CO can be used for comparison. Both molecules are assumed to have a Boltzmann distribution of level populations at 35 K for which

$$\frac{N(HCO^+)}{N(^{13}CO)} = 5.6 \times 10^{-3} \frac{T_R(HCO^+, J = 1\text{–}0)}{T_R(^{13}CO, J = 2\text{–}1)},$$

where the use of a T_R scale corrects for the differences in beam size but not for clumping within that beam. Clumping will affect the results only if there are large differences between the HCO^+ and ^{13}CO distributions. Modest uncertainty is introduced by the slightly different beam sizes, and there is perhaps a half an order of magnitude uncertainty from the expected deviations from a Boltzmann level distribution. Over a 6 km s^{-1} wide interval in both the red and blue HCO^+ and ^{13}CO wings (excluding any core absorption features) the ratio of line intensities is $T_R(HCO^+, J = 1\text{–}0)/T_R(^{13}CO, J = 2\text{–}1) = 0.5$–1.0. This results in an abundance ratio of $X(HCO^+)/X(^{13}CO) = 3$–6×10^{-3}. Using this method to analyze the high-velocity flow in OMC-1, Kuiper, Zuckerman, and Rodriguez-Kuiper (1981) find $X(HCO^+)/X(^{13}CO) = 1 \times 10^{-2}$, and Wootten *et al.* (1984) find 1.4×10^{-2} for the NGC 2071 high-velocity outflow. Wootten *et al.* (1984) used this technique on a number of cold and warm quiescent cloud cores and a pair of supernova remnants. They find that $X(HCO^+)/X(^{13}CO)$ ranges from 2×10^{-2} to 4×10^{-2} in four cold (< 20 K) cloud cores and from 1×10^{-2} to 4×10^{-2} in nine warm (> 20 K) cloud cores (the quiescent material in Cep A has 1.8×10^{-2}), not unlike the values found in the molecular outflows. If the ^{13}CO abundance is unaltered by the passage of a shock, then the HCO^+ abundance is *not* enhanced and is possibly depressed in molecular outflows. In contrast, the $X(HCO^+)/X(^{13}CO)$ toward the supernova remnants is larger than 10^{-1}, probably as a result of enhanced cosmic-ray ionization. If $X(^{13}CO) = 10^{-6}$ is assumed, then the high-velocity flow in Cep A has $X(HCO^+) = 3$–6×10^{-9}.

The electron abundance, x_e, of the high-velocity flow can be estimated from the HCO^+ to CO abundance ratio using the procedure given by Wootten, Snell, and Glassgold (1979). For a flow density of 7×10^5 cm^{-3} and $T_k = 35$ K and the rate constants given by Wootten *et al.*; $x_e = 10^{-8}$ in the Cep A high-velocity flow. The major uncertainty is the appropriate T_k to be used. Higher values of T_k lead to larger ionization levels. A value of $x_e \sim 10^{-8}$ is also found in undisturbed molecular clouds. The derived physical conditions suggest that dense clumps swept up by the outflow have unaltered ionization levels.

d) *Clumping within the Flow*

Determining the location of the high-density high-velocity gas is important to the understanding of the nature of the outflow. Deconvolving the beam from the observed extent of the integrated $J = 1$–0 HCO^+ wing intensity from Figure 5 leads to projected dimensions of 0.43×0.24 pc for the blue lobe and 0.63×0.24 pc for the red lobe. The flow may be unresolved in the direction transverse to the flow axis. The true dimension along the axis of the flow is underestimated because of the unknown inclination angle, which for simplicity is assumed to be 45°. The line-of-sight path length through a cylindrically symmetric lobe is 0.34 pc, assumed to apply to all velocities.

For optically thin emission the total HCO^+ column density is $N(HCO^+) = 9.8 \times 10^{13} \Delta V(\text{km s}^{-1}) T_R(J = 1\text{–}0, HCO^+)/T_{EX}$. Using $T_{EX} = 35$ K for the core position in Figure 5, the column density of high-velocity gas, $N(HCO^+)$, is 2.0×10^{13} cm^{-2} in the blue wing and 1.9×10^{13} cm^{-2} in the red wing. The column density of high-velocity HCO^+ in the vicinity of the HH objects (2'W of the core) is one-third to one-half what it is at the core. The column density of high-velocity HCO^+ can be converted to an average volume density using $X(HCO^+) = 7 \times 10^{-9}$ and by assuming that the line-of-sight dimension of the high-velocity gas is the same as the transverse dimension of the lobe, 0.34 pc. The beam-averaged density of the high-velocity gas is then 2.6×10^3 cm^{-3} at the core. To reconcile this low density with the density of 7×10^5 cm^{-3} required to achieve the relative excitation of the $J = 1$–0 and $J = 3$–2 HCO^+ high-velocity wings requires a volume filling factor of 0.004. Assuming fully thermalized HCO^+ and an average observed line wing intensity of 0.25 K gives a similar filling factor of $T_R(HCO^+)/T_k = 0.007$. This means that the

high-velocity gas in the core is confined to a much smaller volume than implied by the lobe size. The high-velocity gas at the core could be spatially restricted to a single unresolved region, with dimension 10^{-3} pc. The column density and volume density toward the center of the high-velocity lobes are reduced by a similar factor relative to the core of the cloud, and a small (~ 0.01) filling factor is also appropriate there. The intermediate-velocity gas is spatially extended and must come from a number of separate clumps or an unresolved thin jet.

For the case of a beam randomly filled with uniform clumps, the minimum volume filling factor implies a clump size of $R_{\rm CLUMP} = f^{1/3} R_{\rm LOBE}$, 0.02–0.03 pc. This is similar to the size scale (0.01 pc) typical of compact Herbig-Haro objects (Herbig 1969), and the density required for the HCO^+ excitation is consistent with estimates for HH objects. Alternatively, if the high-velocity gas were confined to a narrow unresolved jet, the minimum jet diameter would be 10^{-3} pc (0".3).

e) Flow Energetics

It is instructive to calculate the mass, momentum, and energy of the molecular flow as a function of velocity. These parameters of the flow energetics are calculated for each of the velocity intervals shown in Figure 4. Table 6 tabulates the deconvolved dimensions of the lobe, the flow time scale, the mass, mass flow rate, kinetic energy, and momentum in each velocity zone. An uncertainty is the actual lobe size, since it appears to be unresolved in one dimension. The flow time scale, $t_{\rm AXIAL}$, decreases with increasing velocity when the semi-major dimension is used for the size scale. Most of the flow mass is found at low projected velocities, so the total mass estimate is very sensitive to the subjective integration limits. Equal masses are contained in the corresponding red and blue velocity intervals. The mass accumulation rate $M(M_\odot)/t_{\rm AXIAL}$ decreases by a factor of 3–4 from the lowest to the highest velocity zone. This differs from a similar analysis of the molecular flow in NGC 2071 (Wootten *et al.* 1984), where this rate is constant with velocity. This may reflect a difference in evolutionary state or geometry of the flow. The kinetic energy in the three lowest velocity zones is nearly constant toward Cep A, with lower energy occurring only for the highest velocity zone. Except for the highest velocity zone, a constant energy $E = 9.3 \times 10^{44}$ ergs per 4.2 km s^{-1} interval is found for the sum of red and blue velocity zones. The constant E indicates an equilibrium between material at different velocities. The flow momentum, P, decreases rapidly with increasing velocity. The total mass in the outflow is 7.5 $M_\odot$ with a flow rate of 1.7×10^{-4} $M_\odot$ yr^{-1}, kinetic energy of 3.2×10^{45} ergs, and momentum of 9×10^{39} g cm s^{-1}.

f) Flow Mass Comparisons

The HCO^+ observations indicate that nearly equal masses are contained in the blue lobe (3.5 $M_\odot$) and the red lobe (4.0 $M_\odot$). In comparison, the CO observations of Ho, Moran, and Rodríguez (1982) result in smaller, unequal masses of 0.4 $M_\odot$ for the blue lobe and 1.6 $M_\odot$ for the red lobe. The high spatial resolution Onsala $J = 1$–0 CO map shows that there is a separate flow in the vicinity of the HH objects, and so the CO-based mass estimates for the Cep A outflow alone are probably more nearly equal. Ho *et al.* overestimate the mass in the red lobe by including the 5 km s^{-1} feature which is due to a foreground or background cold low-density cloudlet, not part of the high-velocity flow (see Appendix). Part of the difference between CO- and HCO^+-based mass estimates can be attributed to Ho *et al.*'s use of a CO abundance $X(\rm CO) = 1.8 \times 10^{-4}$, appropriate to low-density dark clouds (Dickman 1978). Even for modest-density clouds of $\sim 10^4$ cm^{-3} (a minimum density for Cep A from the NH_3 data), Wootten *et al.* (1978) find $X(^{13}\rm CO) = 6 \times 10^{-7}$ or $X(\rm CO) = 5 \times 10^{-5}$ for a terrestrial $^{12}C/^{13}C$ ratio. Frerking, Langer, and Wilson (1982) also find that a lower value of $X(\rm CO) = 8.5 \times 10^{-5}$ is appropriate for dense cloud interiors. The high-velocity gas toward OMC-1 has $X(\rm CO) = 1.2 \times 10^{-4}$ (Storey *et al.* 1981; Watson 1982). Using these lower $X(\rm CO)$ values increases mass estimates based on CO by a factor of 1.5–3.5, bringing them closer to the estimates based on HCO^+.

VI. DISCUSSION

Having determined some of the physical conditions appropriate to the outflow gas and the dense core, we can infer the

TABLE 6

CEPHEUS A OUTFLOW ENERGETICS

Velocity Interval	Displacement from Line Center (km s^{-1})	$r_{\rm AXIAL} \times r_{\rm TRANS}$ (pc) × (pc)	$T_{\rm PEAK}$ (K)	$t_{\rm AXIAL}$ (10^4 yr)	M ($M_\odot$)	$M/t_{\rm AXIAL}$ (10^{-5} $M_\odot$ yr^{-1})	E (10^{44} ergs)	P (10^{39} g cm s^{-1})
−30.2 → −26.0	−16.8	0.07 × 0.07	0.2	0.4	0.04	1.0	1.2	0.13
−26.0 → −21.8	−12.6	0.30 × 0.10	0.37	2.3	0.40	1.7	6.3	1.00
−21.8 → −17.6	−8.4	0.17 × 0.12	0.7	2.0	0.58	2.9	3.9	0.97
−17.6 → −13.4	−4.2	0.24 × 0.17	1.5	5.5	2.44	4.4	4.3	2.0
Blue lobe total					3.5	10.1	15.7	4.1
−9.2 → −5.0	4.2	0.38 × 0.21	0.9	8.8	2.92	3.3	5.2	2.4
−5.0 → −0.8	8.4	0.38 × 0.09	0.55	4.4	0.76	1.7	5.4	1.3
−0.8 → 3.4	12.6	0.41 × 0.04	0.3	3.2	0.19	0.6	3.0	0.48
3.4 → 7.6	16.8	0.17 × 0.07	0.2	1.0	0.10	1.0	2.6	0.32
Red lobe total					4.0	6.6	16.2	4.5
Blue + red	16.8				0.14	2.0	3.8	0.5
Blue + red	12.6				0.6	2.3	9.3	1.5
Blue + red	8.4				1.3	4.6	9.3	2.3
Blue + red	4.2				5.4	7.7	9.4	4.4
Total					7.5	16.7	31.9	8.6

properties of the stellar wind that drives the flow and the geometry of the dense quiescent material which channels the flow.

a) Stellar Wind Properties

The parameter $V_{\rm WIND}$, the velocity of the stellar wind, is needed to deduce other parameters of the driving wind. Because of deceleration in the outflow, even the highest velocities in the HCO^+ emission may be considerably less than $V_{\rm WIND}$. The radial velocities and proper motions found for HH objects associated with stellar wind sources indicate that $V_{\rm WIND} \sim 200$ km s^{-1} is typical for energetic outflows; this value is used for Cep A. If momentum is conserved, as the stellar wind impacts the molecular gas, then the mass loss rate of the stellar wind is

$$\dot{M} = \frac{M_{\rm TOTAL}}{t}\left(\frac{V}{V_{\rm WIND}}\right),$$

where $M_{\rm TOTAL}$ is the total mass of swept-up molecular gas, and V and t are the characteristic velocity and time scale in the molecular flow. If all of the high-velocity HCO^+ is attributed to a single source, the total mass loss rate is $1.1 \times 10^{-5}\ M_\odot$ yr^{-1}, equally distributed in each lobe. This value would be reduced by a small fraction if part of the outflow is produced in the secondary outflow source located near the HH objects.

The mechanical luminosity L_w, or kinetic energy flow rate of the stellar wind, is

$$L_w = \tfrac{1}{2}\dot{M}V_{\rm WIND}^2 = 79\dot{M}(M_\odot\ {\rm yr}^{-1})[V_{\rm WIND}({\rm km\ s}^{-1})]^2\ .$$

The blue lobe contributes 18.9 $L_\odot$ and the red lobe 15.5 $L_\odot$ for a total of 34.4 $L_\odot$ generated in the stellar wind sources embedded in Cep A. This represents only a tiny fraction ($\sim$0.1%) of the cluster's radiative luminosity ($2.5 \times 10^4\ L_\odot$, Koppenaal *et al.* 1979), and the embedded sources can easily power the observed stellar wind. A summary of the physical properties derived for the Cep A outflow is given in Table 7.

b) Collimation of the Flow

The bipolar appearance of the high-velocity gas results from collimation of the outflow. With the angular resolution of the current observations, the answer to the question of how close the collimation occurs to the stellar wind source can only be inferred. The HCO^+ observations reveal the presence of high densities confined in a small volume toward the Cep A core. The geometry of the dense core could serve to confine or redirect an initially isotropic flow. If the high-density core has the form of a rotationally flattened disk, the high-velocity flow will be directed along the polar axes. Evidence for a rotating disk is found toward several other molecular outflows. Toward the core of Mon R2 (Loren 1977, 1981*a*) and of NGC 2071 (Bally 1982; Wootten *et al.* 1984), line center velocity gradients occur that are interpreted as disk rotation. As expected, the bipolar high-velocity molecular lobes lie along the rotational axis. The evidence is not as clear-cut for the disklike structure in the HCO^+ observations toward Cep A. There is some flattening of the molecular distribution perpendicular to the apparent high-velocity flow axis (e.g., Fig. 4, *center panel*). The difficulty is that the gradient in the $J = 3$–2 HCO^+ or $H^{13}CO^+$ line center velocity is not in the expected orientation for a rotating disk; a gradient of 2.2 km s^{-1} pc^{-1} is found in an east-west direction, while the rotating disk should produce a north-south gradient. When the high-velocity gas in the vicinity of the HH objects is regarded as a separate outflow, the spatial distribution appears much less bipolar in the Cep A outflow source. The actual velocity gradient may then be due to a disk rotating about a north-south axis. The OSO CO observations (Fig. 5*c*) are, at best, compatible with a NW-SE rotational axis. An alternate explanation for the observed velocity gradient is that it represents high-density clumps in the outflow at low projected velocity, rather than the confining quiescent material.

In other clouds, there is also evidence of collimation of the flow on small scales much closer to the outflow source. Infrared polarization indicates the presence of a flattened circum-

TABLE 7

PHYSICAL CHARACTERISTICS OF THE CEPHEUS A OUTFLOW

Parameter	Blue Lobe	Red Lobe	Combined
Deconvolved projected linear dimensions (pc)	0.43 × 0.24	0.63 × 0.24	...
Assumed lobe thickness (pc)	0.24	0.24	...
$r_{\rm axis}$ (projected distance in pc to the center of the lobe)	0.22	0.32	...
Peak $\int T_R(J = 1\text{–}0, HCO^+)\,dv$ (K km s^{-1})	7.4	6.8	...
$N(HCO^+)$ (cm^{-2})	2.0×10^{13}	1.9×10^{13}	...
$X(HCO^+)$	...	...	7.3×10^{-9}
x_e	...	...	$\lesssim 10^{-8}$
$n(H_2)$ (cm^{-3})	2.7×10^3	2.5×10^3	2.6×10^3
$M_{\rm TOTAL}$ ($M_\odot$)	2.6	3.5	6.1
V (km s^{-1}) (mean velocity)	10	10	...
t (yr) (expansion age)	2.2×10^4	3×10^4	2.6×10^4
M/t (mass accumulation rate)	1.2×10^{-4}	9.8×10^{-5}	2.2×10^{-4}
V_w (km s^{-1}) (assumed wind velocity)	200	200	...
M ($M_\odot$ yr^{-1}) (stellar wind mass loss rate)	6.0×10^{-6}	4.9×10^{-6}	1.1×10^{-5}
L_w ($L_\odot$) (stellar wind luminosity)	18.9	15.5	34.4

NOTE.—These values are calculated from the entire range of high velocities in the lobe structure and will differ slightly from values based on the sum of results from individual velocity intervals (see Table 6).

stellar disk around IRS 5 in L1551 (Nagata, Sato, and Kobayashi 1983). Several highly collimated optical jets have been found (Mundt and Fried 1983); the one in the L1551 cloud lies between IRS 5 and one of the molecular outflow lobes. The emission from the ionized gas toward IRS 5 in L1551 (Cohen, Bieging, and Schwartz 1982) is elongated along the axis connecting the high-velocity lobes. The small filling factor of the high-density high-velocity gas seen in HCO^+ toward the core of Cep A is compatible with an interpretation as either a circumstellar disk or a very narrow high-density collimated jet. These interpretations are not unique, and observations of the HCO^+ outflow in Cep A with newer higher angular resolution antennas can help to decide between these or other cases.

c) *Molecular Shock Interfaces*

The velocities observed in the high-velocity flow clearly exceed the sound speed in the molecular gas, and therefore, shocks must form. Unlike the molecular flow in OMC-1, in Cep A there is no evidence of any molecular gas which exceeds the velocity ($V_s \sim 25$ km s^{-1}) at which H_2 and CO would dissociate in a nonmagnetic shock (Hollenbach and McKee 1980). Draine (1980) found that shocks with magnetic precursors had greater radiative cooling and therefore higher molecular shock velocities than nonmagnetic shocks. The condition for the formation of a magnetic precursor is $B_0^2/\pi\rho_{i0} > V_s^2$, where B_0 is the preshock transverse magnetic field, and ρ_{i0} is the preshock ion density. The formation of a magnetic precursor requires only a modest magnetic field in a region of low fractional ionization, such as found in both the dense core and high-velocity outflow in Cep A. If a magnetic precursor can form easily in the Cep A flow, then the observed terminal velocities probably represent the true maximum velocities in the swept-up molecular gas rather than the dissociation velocity.

There are two diagnostic probes that are sensitive only to the shock-heated gas. The first is vibrationally excited H_2 emission at 2.1 μm, and the second is emission from specific optical lines from low-excitation forbidden transitions which characterize the nebulosity of HH objects (Dopita 1978). Toward Cep A, strong 2.1 μm H_2 emission is found only toward the center of the blueshifted high-velocity lobe (Bally and Lane 1982). The apparent absence of H_2 emission toward the redshifted gas has been attributed to greater 2 μm extinction toward the receding gas. Any optical emission lines might be expected to coincide with the approaching high-velocity gas where the H_2 emission is strongest because extinction is greater at 2 μm than at visual wavelengths. Unexpectedly, the only strong optical line emission from the shock is found toward the redshifted molecular lobe, while none is seen where the H_2 emission is found. No H_2 measurements are available at the position of the HH objects, but no H_2 emission is seen slightly to the north of the HH objects (Bally and Lane 1982). The observed HH object emission lines have large blueshifted radial velocities (-100 to -200 km s^{-1}, Levreault 1982), indicating that they are *not* coincident with the redshifted molecular gas that lies along the same line of sight. The most probable explanation is that both HH object emission and redshifted molecular gas occur on opposite sides of a second bipolar outflow source, but other possibilities cannot be ruled out.[9] The infrared sources (Lenzen and Hefele 1982) and radio continuum source (Hughes and Wouterloot 1982) may be the energy sources which drive a separate molecular outflow in the vicinity of the HH object emission. The high-resolution CO observations also support the idea of a secondary outflow source near the HH objects.

VII. SUMMARY

The detections of spatially extended high-velocity wings in the $J = 1$–0 and $J = 3$–2 HCO^+ lines toward Cep A (this paper) and NGC 2071 (Wootten *et al.* 1984) represent the first density determinations of the high-density clumpy component embedded in bipolar molecular outflows. To summarize the HCO^+ results for the Cep A cloud, we find that:

1. The high-velocity HCO^+ emission has a bipolar spatial distribution with redshifted and blueshifted lobes occurring on opposite sides of the dense core of the cloud where an infrared cluster, H_2O and OH masers, and radio continuum sources are located. At all velocities the strongest HCO^+ emission occurs at the core. At the very highest velocities the HCO^+ emission is detected only at the core. Only at intermediate velocities is the bipolar HCO^+ emission pattern evident, and while it is similar to the CO emission pattern (Ho, Moran, and Rodríguez 1982), the HCO^+ emission does not extend as far to the NW of the core.

2. The intensities of the high-velocity emission in the $J = 1$–0 and $J = 3$–2 HCO^+ lines are compared with statistical equilibrium LVG models to find that a density of $\sim 10^6$ cm^{-3} is required in the outflow material.

3. Comparison of the high-velocity HCO^+ column density and the density required to excite the $J = 3$–2 relative to the $J = 1$–0 HCO^+ emission reveals that the high-density high-velocity component arises from only a small fraction of the volume of the outflow region. A minimum volume filling factor is 0.007 for the 10^6 cm^{-3} high-velocity component.

A similar LVG analysis at the center of the optically thin $J = 1$–0 and $J = 3$–2 $H^{13}CO^+$ lines yields a core density of 7.5×10^5 cm^{-3}. The disparity of the density estimates between $H^{13}CO^+$ and NH_3, for the core, also requires clumping ($f > 0.03$) within the core region.

4. The HCO^+ abundance in the high-velocity material is $X(HCO^+) = 3$–6×10^{-9}, indicating that there is no large increase or decrease of HCO^+ abundance compared with more quiescent regions.

5. The ionization levels are low ($x_e \leq 10^{-8}$) in both the high-velocity gas and the quiescent cloud. Magnetic precursor shocks (Draine 1980) can form under such conditions and moderate the shock temperature.

6. The energy deposited in the flow is roughly constant with velocity, decreasing only at the very highest velocities. The mass and momentum of the flow decrease with increasing velocity. The molecular outflow has a total mass of 7.5 $M_\odot$, an energy of 3×10^{45} ergs, and a momentum of 9×10^{39} g cm s^{-1}. Therefore, it appears that as the flow evolves, it decelerates, sweeping up fresh material.

7. Unexpectedly, a nebulosity found in the direction of the high-extinction region of the redshifted molecular gas has very

[9] One possible geometry in which both the blueshifted HH object emission and redshifted molecular gas arise along the same line of sight requires the Cep A flow axis to have a modest inclination to the plane of the sky. If the flow is not highly collimated, some of the material that is accelerated outward near the equatorial plane, toward the observer, will possess negative radial velocities. The redshifted HCO^+ emission comes predominantly from the high-density clumps in the axial flow, while the weak blueshifted HCO^+ emission and the HH object emission come from similar clumps in the more nearly equatorial flow. An obvious test of this picture is whether 2 μm H_2 emission is detectable at the position of the HH objects.

blueshifted emission lines of the type found in HH objects (Levreault 1982). The presence of an optical spectrum characteristic of a shocked outflow region and the separation of the high-velocity gas into two spatial maxima in our HCO^+ maps and in our OSO CO maps suggest a separate, less energetic outflow source in the western part of the cloud.

The HCO^+ observations have been shown to be ideal probes of the high-density clumps and ionization levels in the outflow regions. The higher J transitions of this abundant molecule and the less abundant isotopic species are unaffected by low-density foreground material and can therefore detect the higher density component of the otherwise partially obscured cloud core where the outflow is collimated.

This work was supported by NSF grant AST 81-16403 to The University of Texas at Austin and by the Swedish Natural Science Research Council. A. W. received partial support from the California Institute of Technology and is grateful to the Dudley Observatory for a Dudley Award and to the Stockholm Observatory for their hospitality. The high-frequency receiver used at MWO was constructed by N. Erickson with support from the NSF to the University of Massachusetts. We would like to thank an anonymous referee for a large number of constructive comments which have greatly improved this paper.

APPENDIX

CO VELOCITY STRUCTURE

While HCO^+ emission provides a probe sensitive to the high-density portions of the cloud, CO observations detect additional velocity components which may arise either in low-density portions of the cloud or in unrelated material along the line of sight. Since CO emission is more spatially extended than HCO^+ emission, the nature of the velocity field of the cloud from which the stars formed can be determined by examining regions removed from the high-velocity flow.

Like so many regions of star formation, the Cep A complex shows evidence for a multiplicity of closely spaced CO velocity components along the line of sight (Sargent 1977). Foreground absorption can make it difficult to clearly distinguish these velocity components. From observations of optically thin NH_3 lines, Brown *et al.* (1981) find evidence for two velocity components in the core region, at velocities of -10.3 and -12.1 km s^{-1}. These components also appear in the $J = 1$–0 ^{13}CO spectrum (Loren *et al.* 1981). The $J = 2$–1 ^{13}CO spectrum at the same position shows less evidence for two components; perhaps because of the higher optical depth of the $J = 2$–1 transition, the separate components are blended into the observed single peak at -11.1 km s^{-1}.

We have observed a few selected positions in the $J = 2$–1 CO and ^{13}CO lines to determine the nature of the various velocity components in Cep A. In the $J = 1$–0 CO line profile toward the core of Cep A, Ho, Moran, and Rodríguez (1982) detected a weak feature at $V_{LSR} = 5$ km s^{-1} superposed on the high-velocity emission. They assigned this component to a high-density clump in the mass outflow. Our CO observations do not support this interpretation. In Figure 7 the $J = 2$–1 CO and ^{13}CO lines observed toward the core position are shown. There is no evidence for the 5 km s^{-1} feature in the $J = 2$–1 CO line profile above the smooth sloping level of the high-velocity wing emission. The typical ratio of 2–1/1–0 line intensity in other high-velocity sources is ~ 1 (Loren *et al.* 1981; Plambeck, Snell, and Loren 1983). The 2–1/1–0 ratio (R) at the 5 km s^{-1} feature, toward Cep A, is less than unity since the 2–1 line does not have a spike of intensity comparable to the 1–0 line. For a hot optically thin gas the ratio R approaches a value of 4 (Goldsmith, Plambeck, and Chiao 1975). For an optically thick gas the ratio would be about 1. A value of R less than unity can occur only for cold (< 10 K) optically thin CO emission. A clump embedded in the high-velocity outflow might have a higher temperature from shock heating, and the CO should be more nearly thermalized because of the higher density. From the low value of R in the 5 km s^{-1} feature we conclude that it is a cold, optically thin, low-density cloudlet that is not associated with the high-velocity flow, but lies, accidentally, along the same line of sight. By including this 5 km

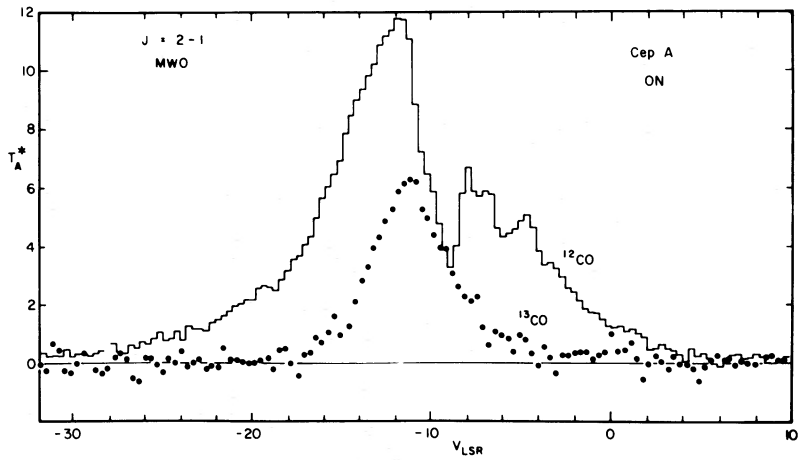

FIG. 7.—The profiles for the $J = 2$–1 CO and ^{13}CO lines toward the core of Cep A. The baseline for the CO profile was determined from the data in wider filters (Fig. 1). There are self-absorption features at $V_{LSR} = -9.5$ km s^{-1}, $V_{LSR} = -6$ km s^{-1}, and possibly at $V_{LSR} = -7.5$ km s^{-1}.

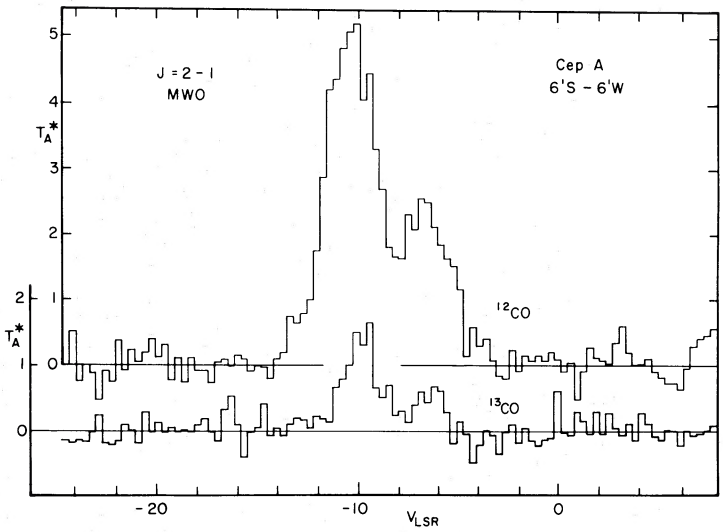

FIG. 8.—The $J = 2$–1 CO and ^{13}CO lines toward a position 6′S-6′W of the core of Cep A which shows emission at two velocities; the higher velocity component coincides in velocity with one of the self-absorption features seen toward the core.

s^{-1} feature in their mass estimate for the high-velocity gas, Ho, Moran, and Rodríguez (1982) overestimate the mass in the redshifted CO lobe.

Ho, Moran, and Rodríguez (1982) state that the self-absorption in the $J = 1$–0 CO line is spatially confined to the redshifted CO lobe. The presence or absence of self-absorption is best determined by a comparison of the profiles of the CO and ^{13}CO lines since dips in the CO profile could also result from multiple velocity components. This kind of comparison showed that self-absorption occurs over the central 6′ of the Cep A core, in the east-west direction (Loren 1981*b*). Figure 8 shows the $J = 2$–1 CO and ^{13}CO line profiles at a position 6′S-6′W of the dense core of Cep A, far outside the redshifted CO lobe. The shape of the CO profile might suggest self-absorption at -8.5 km s^{-1}, but this is not the case. Comparing the CO and ^{13}CO profiles shows that there are two velocity components present at -10 km s^{-1} and -6.5 km s^{-1}. These velocities are close to the velocities of the absorption features at the core position. These components are not restricted to the redshifted lobe but are spatially extended and appear in absorption when seen against the high-velocity hot core emission and in emission at positions away from the core.

We conclude that the complexity of the low-density material along the line of sight to the Cep A complex complicates the CO estimates of mass of the high-velocity outflow. To deduce where extraneous foreground gas is present will require more spatial observations of both CO and ^{13}CO, especially the $J = 2$–1 transitions, which are less affected by low-density gas than the $J = 1$–0 transitions. In contrast to CO observations, our HCO^+ measurements accurately measure the mass of the denser components of the flow.

REFERENCES

Bally, J. 1982, *Ap. J.*, **261**, 558.
Bally, J., and Lane, A. P. 1982, *Ap. J.*, **257**, 612.
Beichman, C. A., Becklin, E. E., and Wynn-Williams, C. G. 1979, *Ap. J. (Letters)*, **232**, L47.
Bogey, M., Demuynck, C., and Destombes, J. L. 1981, *Molec. Phys.*, **43**, 1043.
Brown, A. T., Little, L. T., McDonald, G. H., Riley, P. W., and Matheson, D. N. 1981, *M.N.R.A.S.*, **195**, 607.
Cohen, M., Bieging, J. H., and Schwartz, P. R. 1982, *Ap. J.*, **253**, 707.
Dickman, R. L. 1978, *Ap. J. Suppl.*, **37**, 407.
Dopita, M. 1978, *Ap. J. Suppl.*, **37**, 117.
Draine, B. T. 1980, *Ap. J.*, **241**, 1021.
Elitzur, M. 1983, *Ap. J.*, **267**, 174.
Erickson, N. R. 1981, *IEEE Trans.*, **MTT-29**, 557.
Erickson, N. R., Goldsmith, P. F., Snell, R. L., Berson, R. L., Huguenin, G. R., Ulich, B. L., and Lada, C. J. 1982, *Ap. J. (Letters)*, **261**, L103.
Evans, N. J., II. 1980, in *IAU Symposium 87, Interstellar Molecules*, ed. B. H. Andrew (Dordrecht: Reidel), p. 1.
Evans, N. J., II. *et al.* 1981, *Ap. J.*, **244**, 115.
Frerking, M. A., Langer, W. D., and Wilson, R. W. 1982, *Ap. J.*, **262**, 590.
Garmany, C. 1973, *A.J.*, **78**, 185.
Goldsmith, P. F., Plambeck, R. L., and Chiao, R. Y. 1975, *Ap. J. (Letters)*, **196**, L39.
Green, 1975, *Ap. J.*, **201**, 366.
Gyulbudaghian, A. L., Glushkov, Yu. I., and Denisyuk, E. K. 1978, *Ap. J. (Letters)*, **224**, L137.
Haese, N. N., and Woods, R. C. 1979, *Chem. Phys. Letters*, **61**, 396.
Harten, R. H., Thum, C., and Felli, M. 1981, *Astr. Ap.*, **94**, 231.
Herbig, G. H. 1969, in *Nonperiodic Phenomena in Variable Stars*, ed. L. Detre (Dordrecht: Reidel), p. 75.
Ho, P. T. P., Moran, J. M., and Rodríguez, L. F. 1982, *Ap. J.*, **262**, 619.
Hollenbach, D., and McKee, C. F. 1980, *Ap. J. (Letters)*, **241**, L47.
Hughes, V. A., and Wouterloot, J. G. A. 1982, *Astr. Ap.*, **106**, 171.
Koppenaal, K., Sargent, A. I., Nordh, L., van Duinen, R. J., and Aalders, J. W. G. 1979, *Astr. Ap.*, **75**, L1.
Kuiper, T. B. H., Zuckerman, B., and Rodriguez-Kuiper, E. N. 1981, *Ap. J.*, **251**, 88.
Kutner, M. L., and Ulich, B. L. 1981, *Ap. J.*, **250**, 341.
Lada, C. J., Blitz, L., Reid, M., and Moran, J. 1981, *Ap. J.*, **243**, 769.
Lenzen, R., and Hefele, H. 1982, *Galactic and Extragalactic Infrared Spectroscopy* (ESA SP-192), p. 65.
Levreault, R. M. 1982, unpublished data.
Loren, R. B. 1977, *Ap. J.*, **215**, 129.
———. 1981*a*, *A.J.*, **86**, 69.
———. 1981*b*, *Ap. J.*, **249**, 550.
Loren, R. B., Plambeck, R. L., Davis, J. H., and Snell, R. L. 1981, *Ap. J.*, **245**, 495.
Loren, R. B., and Wootten, H. A. 1980, *Ap. J.*, **242**, 568.
Loren, R. B., Wootten, A., Mundy, L. G., and Peters, W. L. 1984, in preparation.
Mundt, R., and Fried, J. W. 1983, *Ap. J. (Letters)*, **274**, L83.
Mundy, L. G. 1981, unpublished data.
Mundy, L. G., and Loren, R. B. 1984, in preparation.
Nagata, T., Sato, S., and Kobayashi, Y. 1983, *Astr. Ap.*, **119**, L1.
Norris, R. P. 1980, *M.N.R.A.S.*, **193**, 39P.
Olofsson, H., Ellder, J., Hjalmarson, Å., and Rydbeck, G. 1982, *Astr. Ap.*, **113**, L18.
Phillips, J. P., White, G. J., and Watt, G. D. 1982, *M.N.R.A.S.*, **199**, 1033.
Phillips, T. G., Knapp, G. R., Huggins, P. J., Werner, M. W., Wannier, P. G., Neugebauer, G., and Ellis, D. 1981, *Ap. J.*, **245**, 512.
Plambeck, R. L., Snell, R. L., and Loren, R. B. 1983, *Ap. J.*, **266**, 321.
Plambeck, R. L., Wright, M. C. H., Welch, W. J., Bieging, J. H., Baud, B., Ho, P. T. P., and Vogel, S. N. 1982, *Ap. J.*, **259**, 617.

Rodríguez, L. F., Ho, P. T. P., and Moran, J. M. 1980, *Ap. J.* (*Letters*), **240**, L149.
Rodríguez, L. F., Moran, J. M., Ho, P. T. P., and Gottlieb, E. W. 1980, *Ap. J.*, **235**, 845.
Sandqvist, Aa., Loren, R. B., Wootten, A., Friberg, P., and Hjalmarson, Å. 1982*a*, "The Scientific Importance of Submillimeter Observations," preprint, p. 131.
Sandqvist, Aa., Wootten, A., Loren, R. B., Friberg, P., and Hjalmarson, Å. 1982*b*, in *Regions of Recent Star Formation*, ed. R. S. Roger and P. E. Dewdney (Dordrecht: Reidel), p. 307.
Sargent, A. I. 1977, *Ap. J.*, **218**, 736.
Sastry, K. V. L. N., Herbst, E., and DeLucia, F. C. 1981, *J. Chem. Phys.*, **75**, 4169.
Snell, R. L., Loren, R. B., and Plambeck, R. L. 1980, *Ap. J.* (*Letters*), **239**, L17.
Storey, J. W. V., Watson, D. M., Townes, C. H., Haller, E. E., and Hansen, W. L. 1981, *Ap. J.*, **247**, 136.
Turner, B. E., and Thaddeus, P. 1977, *Ap. J.*, **211**, 755.
Ulich, B. L., and Haas, R. W. 1976, *Ap. J. Suppl.*, **30**, 247.
Watson, D. M. 1982, in *Symposium on the Orion Nebula to Honor Henry Draper*, ed. A. E. Glassgold, P. J. Huggins, and E. L. Schucking (*Ann. NY Acad. Sci*, Vol. **395**), p. 136.
Woods, R. C., Dixon, T. A., Saykally, R. J., and Szanto, P. G. 1975, *Phys. Rev. Letters*, **35**, 1269.
Wootten, A., Evans, N. J., II, Snell, R. L., and Vanden Bout, P. A. 1978, *Ap. J.* (*Letters*), **225**, L143.
Wootten, A., and Loren, R. B. 1984, in preparation.
Wootten, A., Loren, R. B., and Bally, J. 1984, *Ap. J.*, **277**, 189.
Wootten, A., Loren, R. B., Sandqvist, Aa., Friberg, P., and Hjalmarson, Å. 1984, *Ap. J.*, **279**, 633.
Wootten, A., Snell, R. L., and Glassgold, A. E. 1979, *Ap. J.*, **234**, 876.

PER FRIBERG: FCRAO, GRC TWR B, University of Massachusetts, Amherst, MA 01003

ÅKE HJALMARSON: Onsala Space Observatory, Onsala S-430 34, Sweden

ROBERT B. LOREN: Department of Astronomy, University of Texas at Austin, Austin, TX 78712

AAGE SANDQVIST: Stockholm Observatory, S-133 00 Saltsjöbaden, Sweden

ALWYN WOOTTEN: NRAO, Edgemont Road, Charlottesville, VA 22901